Supporting Information

Stop-Frame Filming and Discovery of Reactions at the Single-Molecule Level by Transmission Electron Microscopy

Thomas W. Chamberlain, Johannes Biskupek, Stephen T. Skowron, Alexander V. Markevich, Simon Kurasch, Oliver Reimer, Kate Walker, Graham A. Rance, Xinliang Feng, Klaus Müllen, Andrey Turchanin, Maria A. Lebedeva, Alexander G. Majouga, Valentin G. Nenajdenko, Ute Kaiser, Elena Besley, Andrei N. Khlobystov

S1. Perchlorocoronene on graphene.

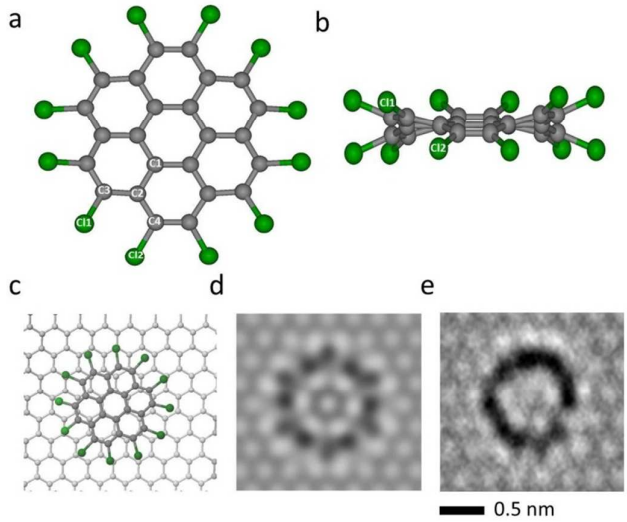

Figure S1. (a) Face-on and (b) edge-on views of the structural diagram of perchlorocoronene (PCC); carbon and chlorine atoms are grey and green respectively. (c) Structural diagram, (d) simulated and (e) experimental 80 kV AC-HRTEM images of PCC on graphene. Note that, in the experimental AC-HRTEM image, the Cl-atoms of the molecule cannot be completely resolved due to thermal vibrations at room temperature and electron beam-induced movements.

S2. Threshold energy & cross-section calculations of PCC.

<u>Cl emission from PCC</u>

The rotation of the PCC molecule in the nanotube results in two orientations relative to the electron beam, shown in Fig S1. In the zig-zag (ZZ) orientation, impacts on two inequivalent atoms of PCC at 80 keV can lead to atom emission; however, these simply correspond to processes accessible when the molecule is in the armchair (AC) orientation, but with energy transferred in suboptimal directions. The preference of the AC orientation of PCC for emission is due to the presence of C-C and C-Cl bonds parallel to the e-beam. Energy can be transferred more efficiently along these bonds to the terminating Cl atoms.

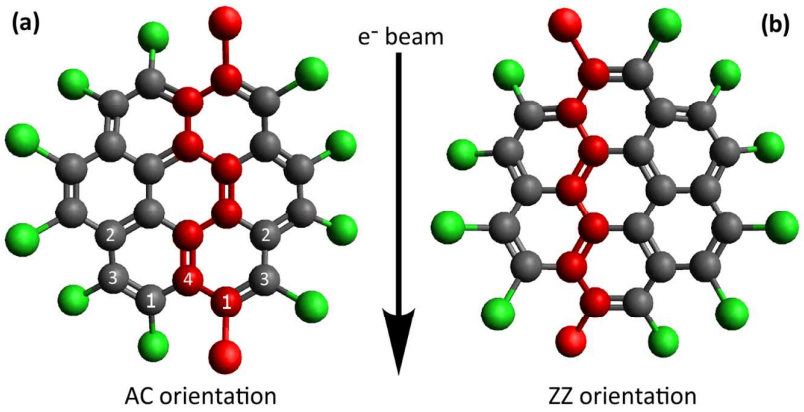

Figure S2. The two extreme orientations of PCC@SWNT relative to the e-beam (direction shown by the arrow), with (a) armchair and (b) zigzag configurations along the beam axis, indicated in red. Impacts with the inequivalent atoms labelled in (a) can lead to atom emission events accessible to the 80 keV electron beam.

There are 4 inequivalent primary knock-on atoms (PKAs) in PCC in the AC orientation for which atom emission is accessible *via* a direct knock-on collision at 80 keV. At this beam energy, the maximum transferrable energy to a stationary carbon atom is 15.8 eV, while the maximum energy transferable to chlorine is only 5.3 eV due to its larger mass. Hence, atom emission is only possible *via* an initial energy transfer to carbon atoms, subsequently leading to the emission of chlorine after this energy is redistributed through the molecule.

Impacts on PKAs (1) or (2) can result in the emission of a single Cl atom, impacts on PKAs (3) can result in the emission of a CCl_2 fragment, and an impact on PKA (4) can result in the emission of two adjacent Cl atoms. For small ranges of transferred energy, Stone-Wales-type bond rotations were also witnessed.[1] Considering all of these avenues of beam induced atom emission and the calculated threshold energies for each process, at 80 keV the total damage cross-section is 159 barn per PCC molecule, corresponding to an electron dose of 6.28×10^7 e^-/nm^2 per molecule, and consisting of 90% Cl emission, 8% CCl_2 fragment emission, and a negligible number of bond rotations and Cl_2 emissions. These results are summarised in Table S1, and the dependence of the cross-section of each process on the beam energy is shown in Figure S2.

Table S1. A summary of the beam induced processes of atom emission for PCC accessible to an 80 keV electron beam, with the threshold energies calculated *via* AIMD simulations. Cross-sections and characteristic doses are given per molecule, at the experimentally used beam energy of 80 keV.

PKA	Result	Threshold energy E_d (eV)	Cross-section σ (b)	Characteristic dose D_c (e^- nm^{-2})	% of damage at 80 keV
(1)	Cl emission	9.1 ± 0.1	127	7.87×10^7	80 %
(2)	Cl emission	14.4 ± 0.1	16	6.25×10^8	10 %
(1) + (2)	**Cl emission**	-	**143**	**6.99×10^7**	**90 %**
(3)	CCl_2 emission	14.7 ± 0.1	12	8.33×10^8	8 %
(4)	Cl_2 emission	15.1 ± 0.1	4	2.50×10^9	3 %
All	**Atom emission**	-	**159**	6.29×10^7	**100 %**

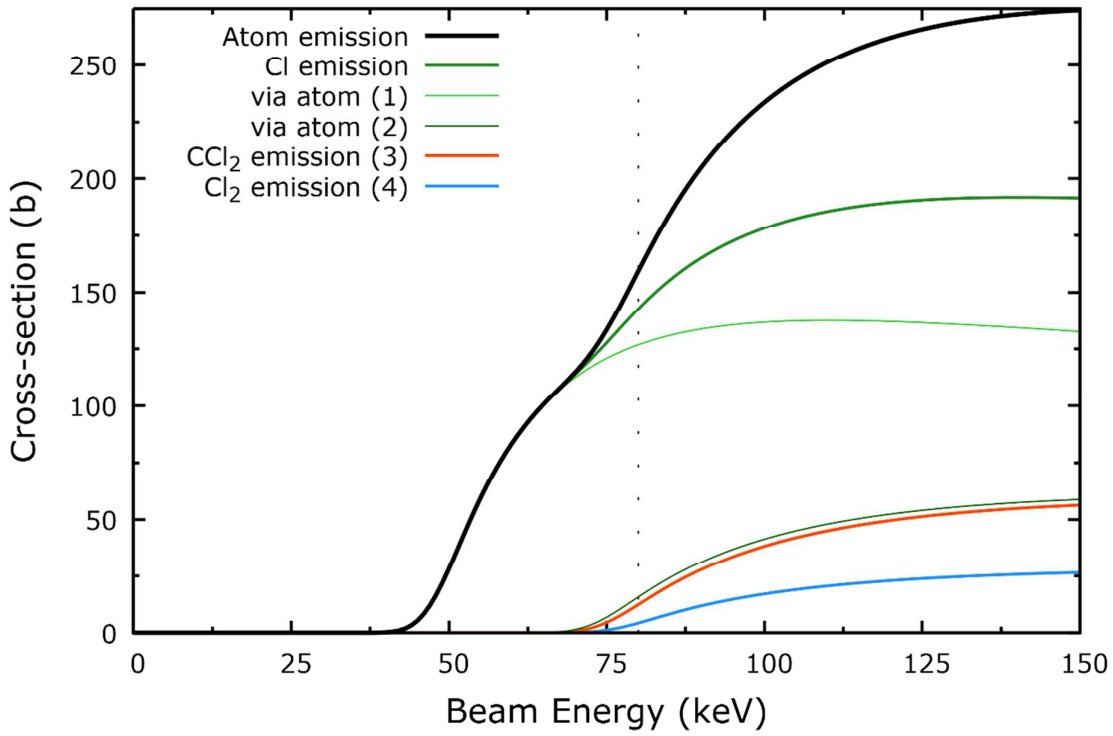

Figure S3. The total emission cross-section, per molecule of PCC, as a function of the electron beam energy. This is broken down into constituent cross-sections for each emitted fragment and for each PKA indicated in Figure S1. The experimental beam energy of 80 keV is indicated by the dotted black line.

Bond breaking of the Diels-Alder adduct

As discussed in the text, the initial adduct formed from the Diels-Alder addition ($C_{48}Cl_{22}$) is kinetically stable; however, due to the collisions of the electrons from the beam, the out-of-plane 'bridging' C-C bond can be broken as shown in Figure S4. The threshold energy for breaking this bond is 10.9 ± 0.1 eV, at which energy the impacted carbon atom and the chlorine atom bonded to it are captured by the edge, leading directly to the reaction pathway shown in Figure S4. Above 13.6 ± 0.1 eV, enough energy is transferred that a CCl_2 fragment is completely emitted from the structure. The reaction will follow the same pathway, but the resulting structure will have an additional carbon atom missing ($C_{47}Cl_{18}$ rather than $C_{48}Cl_{18}$), corresponding to a pentagon in place of the central edge hexagon.

At 80 keV, the overall cross-section for breaking this bond is 76 barn, and the bond breaking accompanied by atom emission has a cross-section of approximately 28 barn. At 80 keV, the planarisation step will therefore be expected to occur after a characteristic dose of 1.32×10^8 e^-/nm, and approximately 27% of planarisation steps will be expected to produce products with a 5-membered ring at this beam energy. This explains the observation that the structures of nanoribbons formed from PCC are not perfect, and often include defects. Figure S3 shows the dependence of this step on the beam energy, and indicates that the final structure of the nanoribbon can be tuned by careful choice of the experimental accelerating voltage; a beam energy of approximately 65 keV is predicted to maximise the rate of this step while resulting in nanoribbons only consisting of hexagons, while above 90 keV the majority of couplings will result in pentagon formation.

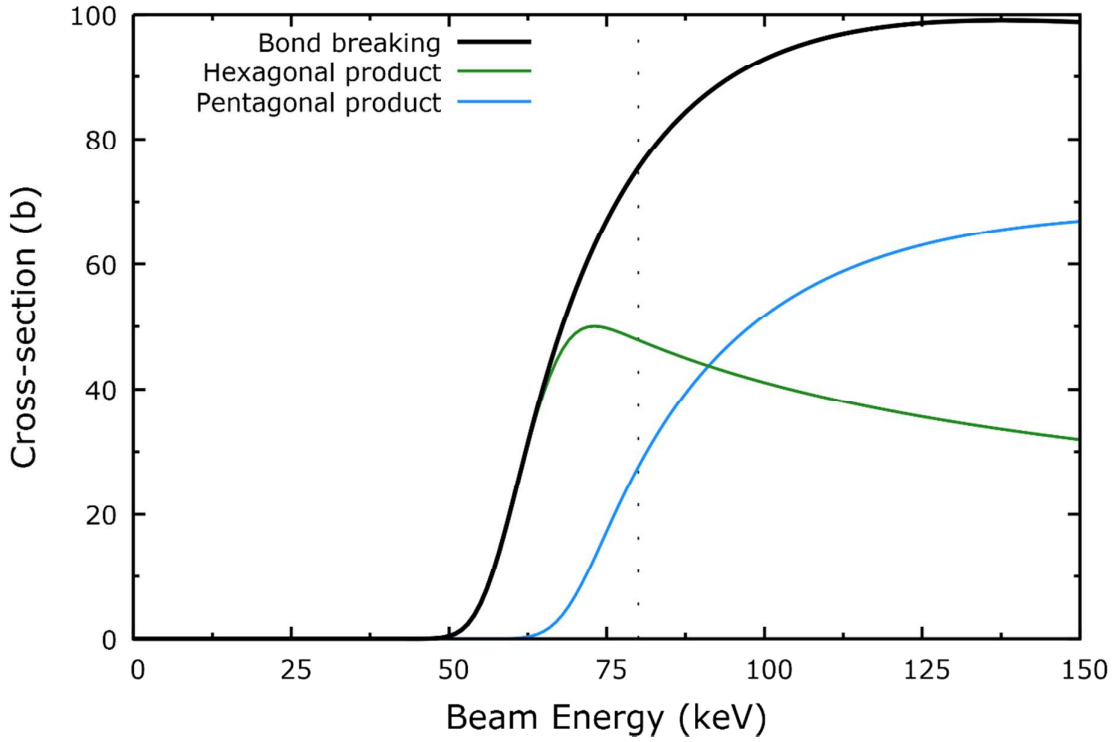

Figure S4. The total cross-section for breaking the bridging C-C bond, per molecule of PCC, as a function of the electron beam energy. Depending on the exact energy transferred, the final structure will either contain a single pentagon or be completely composed of hexagons; the cross-sections for each of these possibilities are also shown. The experimentally used beam energy of 80 keV is indicated by the dotted black line.

S3. Transferred energy from e-beam to atoms.

The maximum kinetic energy, *T*, transferred from the incident electron to a stationary atom can be expressed as;

$$T = \frac{2 \cdot M \cdot E\left(E + 2m_e \cdot c^2\right)}{(M + m_e)^2 \cdot c^2 + 2M \cdot E}$$

where *M* – mass of atoms, m_e – mass of electron, *E* – energy of the e-beam, and *c* – speed of light.[2]

Table S2. The maximum energy that can be transferred from an 80 keV e-beam to an atom

Element	Atomic weight	Maximum energy transferred to an atom from a 80 keV e-beam
C	12	15.8 eV
Cl	35.5	5.3 eV
S	32	5.9 eV

S4. Nanoribbons derived from PCC@SWNT under 80 keV e-beam.

As discussed in the text and shown in Figure 2 the initial transformations from stacks of PCC molecules to well-defined dimers and oligomers can be observed revealing atomic details of the

process inside the SWNT using AC-HRTEM. The subsequent, more complicated transformations of perchlorinated dimers to elongated Cl-GNR can also be observed over time (Figure S5). The images show the formation process after initial dimer formation for the Cl-GNR depicted in Figure 3a in the main manuscript.

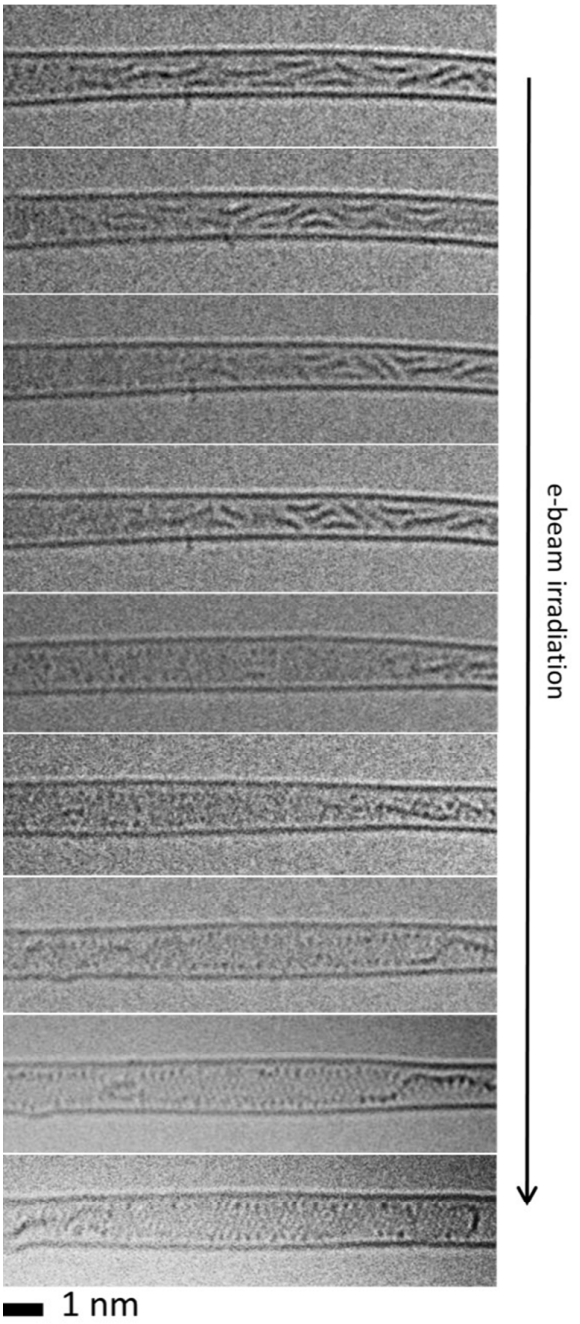

Figure S5. Time series of AC-HRTEM images at 80keV showing a complete sequence of transformations of discrete PCC molecules into a continuous nanoribbon under e-beam irradiation.

The resultant Cl-GNRs, formed by electron beam irradiation, were observed to be stable to further electron beam irradiation and are highly dynamic, rotating inside the SWNT over time, see time series a-e below. The Cl-GNRs rapidly twist inside the SWNT, showing no strong, directional interaction with the nanotube side-wall. In individual images, different protections of the Cl-GNR

can be observed, including face-on where the structure of the plane of the Cl-GNR can be clearly seen (black arrows) and edge-on where the plane of the Cl-GNR is parallel to the direction of the electron beam so the nanoribbon is observed as a single line of dark contrast (white arrows). As a result of the dynamic twisting of the Cl-GNR over time both protections of the same ribbon can be observed over time (Figure S6).

Within a PCC@SWNT stack, each 1 nm of the nanotube length is occupied by 3 PCC molecules with the total number of atoms which equates to 3 x $C_{24}Cl_{12}$ = $\mathbf{C_{72}Cl_{36}}$. In contrast the Cl-GNR occupying 1 nm of the nanotube length has about five Cl-atoms on either side, which considering that the repeating unit of the Cl-GNR backbone is $\{C_8Cl_2\}_n$ equates to 5 x C_8Cl_2 = $\mathbf{C_{40}Cl_{10}}$. This means that the Cl-GNR@SWNT is less dense than PCC@SWNT (mass/volume density). However, nanoribbon twisting inside the nanotube channel may offset the difference in density.

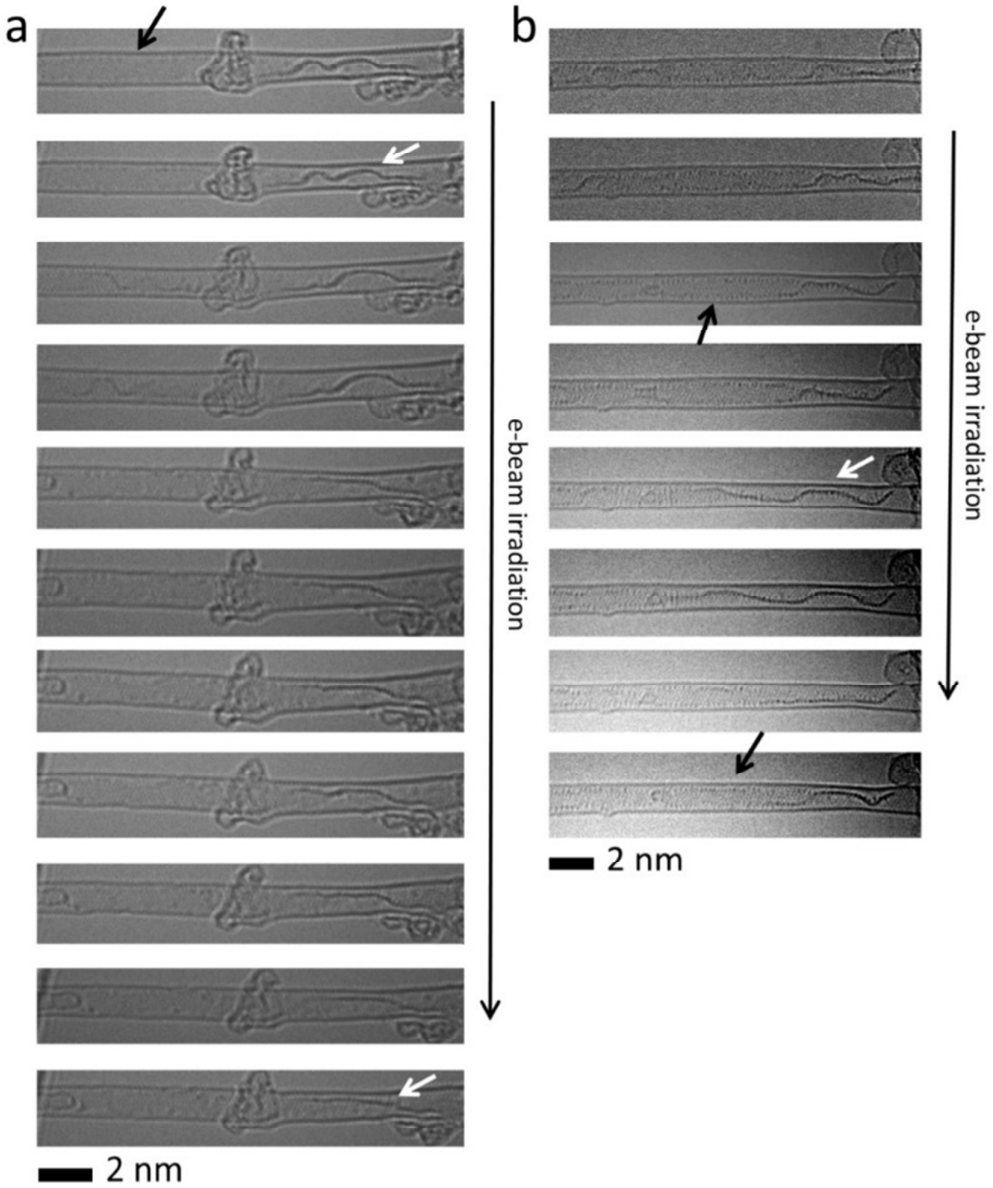

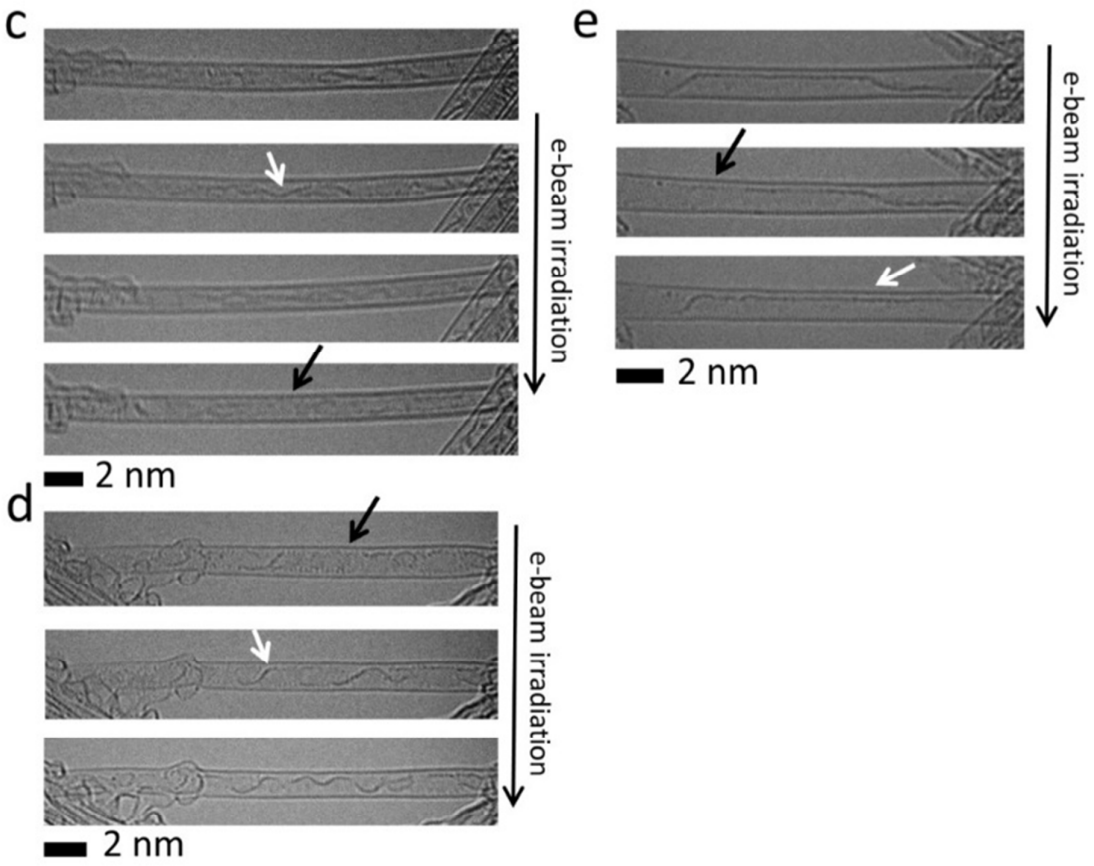

Figure S6. a-e) Time series of AC-HRTEM images at 80keV showing the dynamic behaviour of Cl-GNRs in the e-beam in which different protections of the Cl-GNR can be observed, including face-on where the structure of the plane of the Cl-GNR can be clearly seen (black arrows) and edge-on where the plane of the Cl-GNR is parallel to the direction of the electron beam so the nanoribbon is observed as a single line of dark contrast (white arrows).

S5. Imaging OTC (sulflower) in carbon nanotubes.

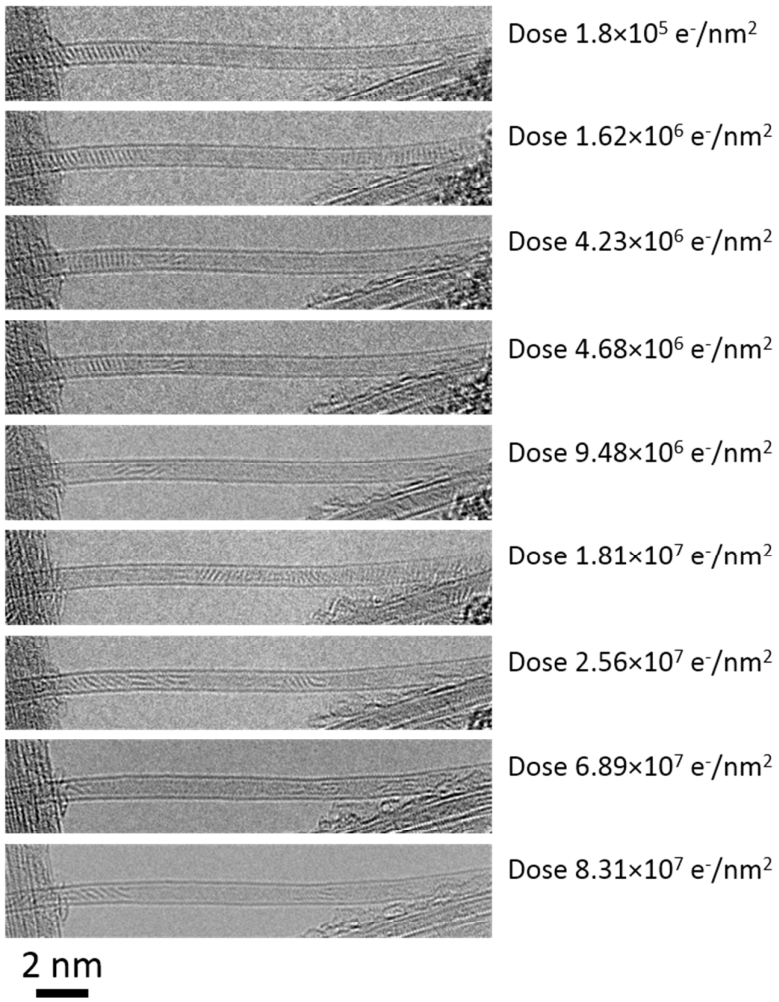

Figure S7. Time series of AC-HRTEM images at 80keV showing a complete sequence of transformations of discrete OTC molecules into a continuous nanoribbon.

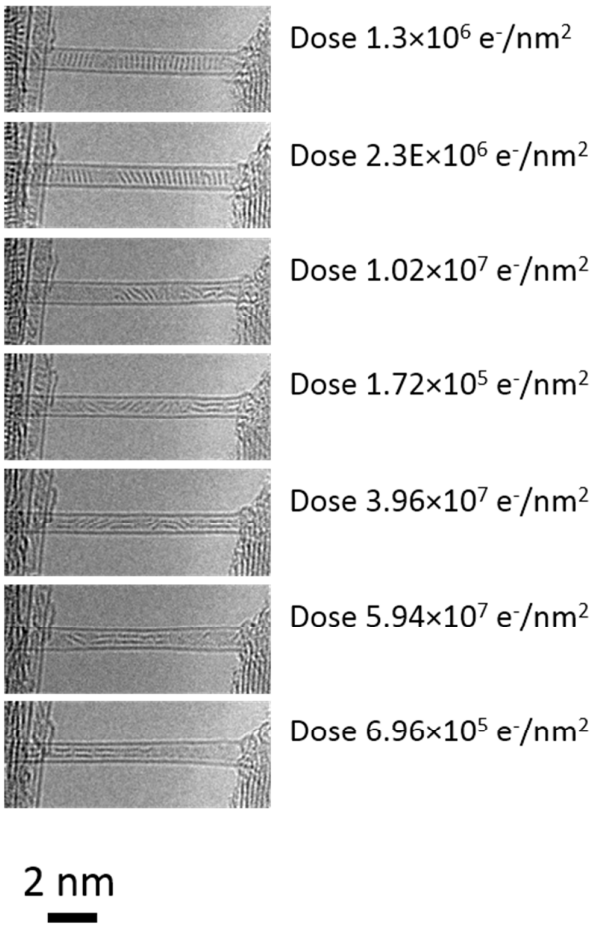

Figure S8. Time series of AC-HRTEM images at 80keV showing a complete sequence of transformations of discrete OTC molecules into a continuous nanoribbon.

S6. Polymeric structures derived from OTC@SWNT under 80 keV e-beam.

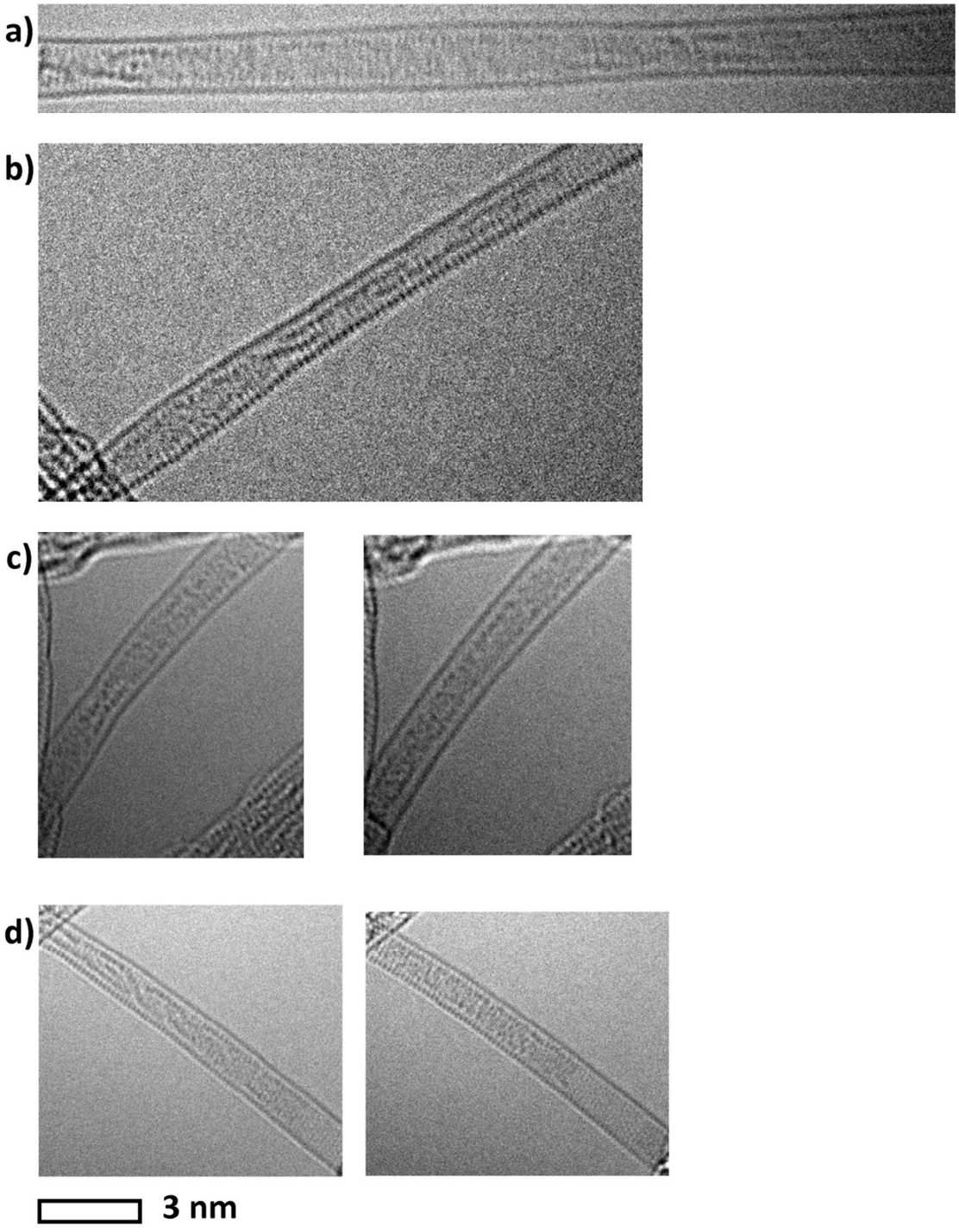

Figure S9. a-d) AC-HRTEM images at 80 keV showing examples of sulphur containing nanoribbons formed by e-beam irradiation of OTC@SWNT.

S7. DFT calculations of reactions of OTC molecules.

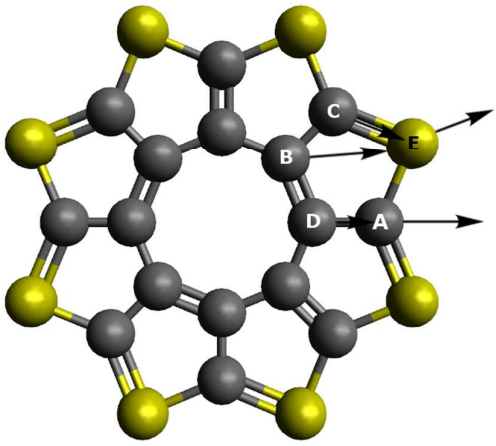

Figure S10. The sulflower molecule octathio[8]circulene, with the inequivalent impacts and their directions indicated.

Initial atom emission and reaction

The highly symmetrical structure of the sulflower means that there are only three atom environments (sulphur, inner carbon, outer carbon) and only five inequivalent high-symmetry impacts with the possibility of structural modification, shown in Figure S10. After the transmission of 15.8 eV to atoms *A* to *D* and 5.9 eV to *E*, reactions were observed to occur for *A* to *C*, but not for *D* and *E*. Following impact *C*, a CS_2 fragment was emitted with a very low kinetic energy, indicating that this energy was very close to the threshold for emission. The remainder of the sulflower molecule rearranged to form a biradical species. For impact *B*, a bond rotation occurred, again forming a biradical species, but without any atom emission. In impact *A*, a carbon atom was easily ejected and retained a very high kinetic energy following emission, implying that the threshold energy for this process is substantially below T_{max}. A biradical species was again formed. These three activations by the beam and subsequent possible reactions with adjacent molecules in the stack are shown in Figure S11. As activation of *A* is readily accessible under the 80 keV beam while the other two reactions will only occur at or around T_{max} (and therefore very rarely), only the consequences of *A* are considered. The three biradical species that are formed are very similar and would be expected to follow the same general mechanism, but will result in slightly different products being formed.

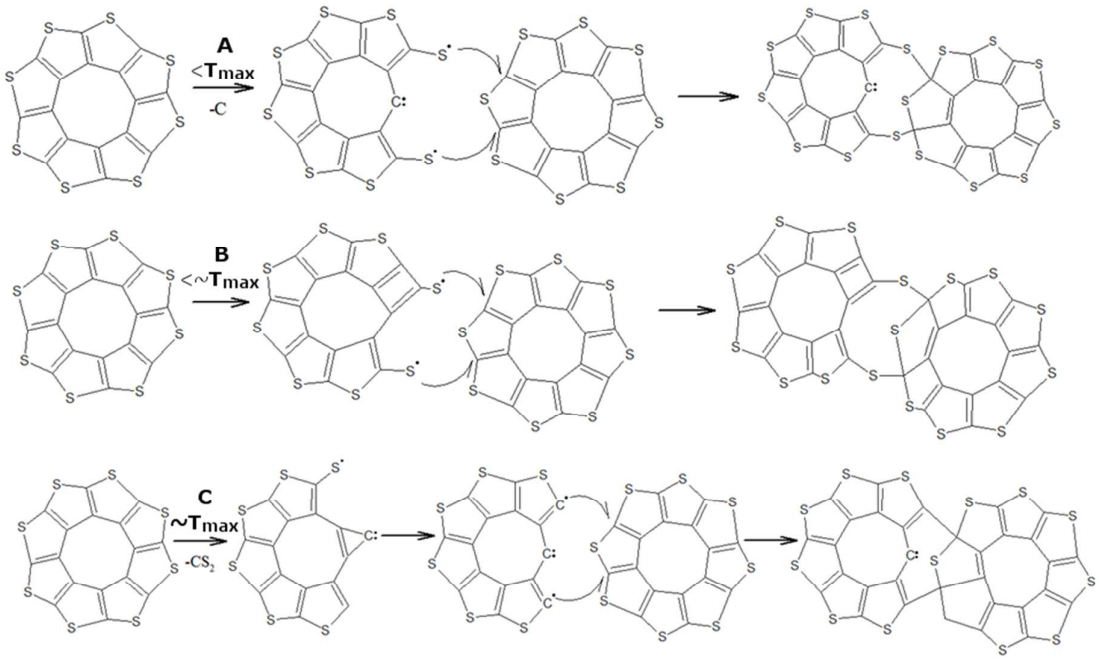

Figure S11. The result of the impacts, shown in Figure S10 after transmission of T_{max}, and subsequent reactions, that are possible with adjacent sulflower molecules. No reaction occurred for impacts *D* and *E*.

The radical driven reaction following impact *A* is not as sterically demanding as the Diels-Alder reaction required for PCC, but should be able to occur in the molecular stacks. In fact, the dimer species formed prefers a U-shaped orientation very similar to that of the parallel stacked molecules, with an angle of 40° between the planes of the molecules, caused by the two sp^3-hybridised carbon atoms bonded to the bridging sulphur atoms. This matches stable structures seen experimentally during the transformation, also shown in Figure 5d, main text.

Subsequent emission and conformational changes

Following the formation of this stable species, two atoms are especially vulnerable to emission *via* a collision with an incident electron: the under-coordinated carbon atom and a sulphur atom, as shown in Figure 5g. The sulphur atom is readily emitted even *via* an energy transfer to the sulphur atom itself, despite the low value of T_{max}, and the carbon atom is also very easily lost with a threshold energy substantially below the T_{max} for carbon. These atom emissions would therefore be expected to happen relatively quickly, but in either order.

After sulphur emission (either as the first or the second step), the structure returns to being fully sp^2-hybridised and a conformational change of the molecule can occur. The two bridging C-S-C bonds begin in a `*cis*' configuration due to the relative orientation of the two precursor molecules, but inversion of one of them leads to a lower energy `*trans*' configuration that allows some degree of planarisation. If the carbon atom is also emitted, the final `*trans*' structure is only slightly non-planar, and is composed of a 7- and 8-membered ring surrounded by thiophene groups, with two bridging sulphur atoms between them.

Although the carbon atom can be emitted, and the sulphur atom emitted so readily that 5.9 eV is substantially more than the threshold energy, at 80 keV an impact at T_{max} on the carbon towards the sulphur does not transfer enough energy to simultaneously emit both. The removal of the two

atoms will therefore occur as a result of two separate collisions, leading to a long time (atomically speaking) between emissions, and so the structures will be fully relaxed into their ground states between impacts. At a higher accelerating voltage, simultaneous emission would be possible and could lead to a rearrangement resulting in the formation of a perfect thiocirculene, similar to the starting material but with a central 15-membered ring (pentadecathio[15]circulene). This could only occur following simultaneous C- and S-emission, as after emitting only one of the atoms the molecule quickly relaxes to a geometry where thiocirculene formation is impossible.

Due to the large internal angle of a [15]circulene, its stable geometry is helical, and adoption of a planar structure similar to those of the nanoribbons that are formed would require a huge amount of strain. It is, however, interesting to note that the original orientation of two adjacent sulflower molecules in the stack is ideal for this preferred helical structure, as well as the intermediate structure shown in Figure 5 - this entire process would not require any rearrangements of the molecular stack, but only very minor adjustments in position. Due to the nanotube confining the sulflower molecules in a coincidentally perfect sterical configuration required for the helical structure of large circulenes, at a higher accelerating voltage the electron beam could in principle drive the formation of arbitrarily large thiocirculenes from molecular stacks of sulflower molecules encapsulated inside carbon nanotubes. As there is no current chemical route towards heterocirculenes of this size despite interest in them,[3] the electron beam could prove to be a very useful tool for the synthesis of this kind of new and interesting one dimensional nanostructure.

Further molecular additions

Considering the structure of the end dimer product shown in Figure 5g with respect to further additions of sulflower molecules, there are only two possible structures for a trimer (assuming that the same mechanism occurs), as the presence of the nanotube limits any further reactions occurring along the same axis of the molecule. One end of the dimer resembles the initial sulflower in the orientation that a carbon atom is emitted from (the left side in this figure), while the other end of the dimer is in the orientation that reacts with the impacted molecule (the right side). Hence, an electron impact emitting a carbon atom from the left of the dimer can react with a new sulflower molecule to form an '8-6-8' species, and the right side of the dimer can react following the emission of a carbon atom from a new molecule to the right of the dimer, to form a '7-8-7' species, shown in Figure S12. Repeating this process, the resulting infinite thiophene nanoribbon will have a '...-8-6-8-6-...' structure in the ideal case.

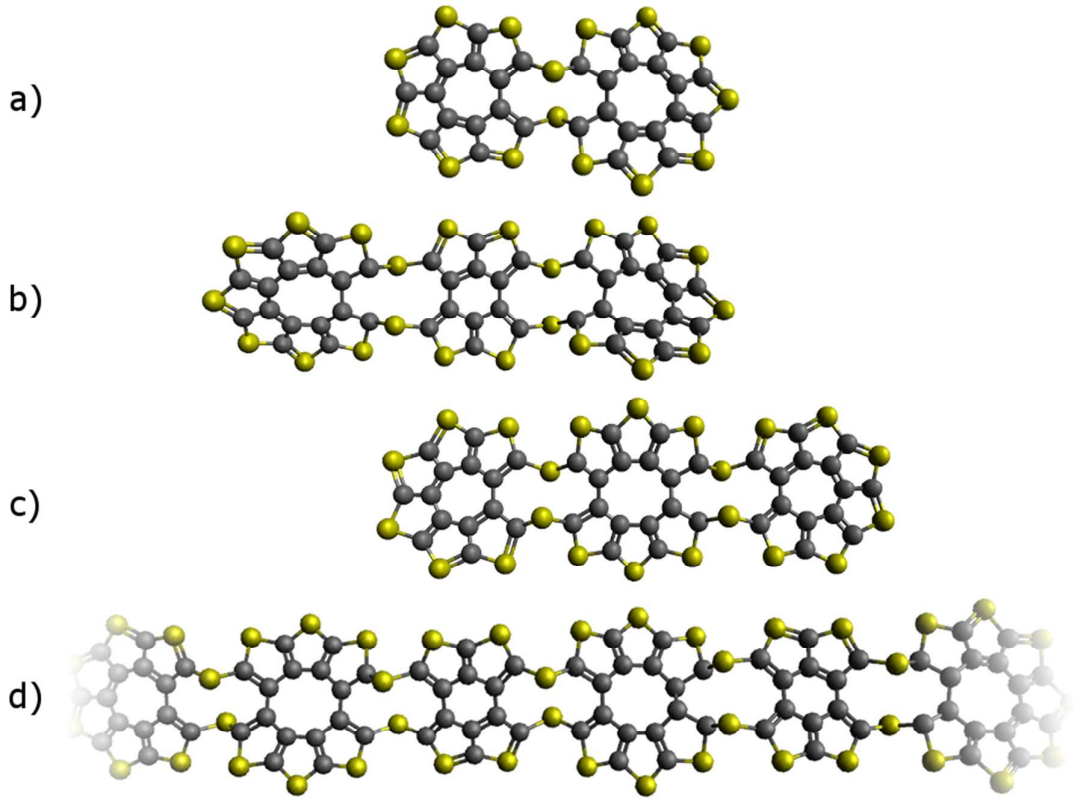

Figure S12. a) The atomic structures of the '7-8' dimer, (b) the '8-6-8' trimer, (c) the '7-8-7' trimer, and (d) the infinite '...-8-6-8-6-...' nanoribbon.

It should be emphasised that these are only the main routes available, composed of the most probable beam-induced steps; under the electron beam large amounts of energy is transferred randomly to different atoms at different angles, resulting in very stochastic processes. A distribution of exact atomic structures will be formed along the ribbons. This is especially the case with the sulflower reactions described here, as in addition to the multiple initiating steps, the end structure will still be vulnerable to atom emission and bond reorganisations from the e-beam, unlike the Cl-terminated graphene nanoribbons. This structure is, therefore, the ideal case, simply the most probable structure formed immediately after polymerisation.

S8. Raman spectroscopy of PCC@SWNT and OTC@SWNT structures.

Experimental

Raman spectroscopy was conducted using a Horiba–Jobin–Yvon LabRAM HR spectrometer, with a laser wavelength of 532 or 660 nm operating at a power of *ca.* 0.5-3 mW and a 600 lines mm^{-1} grating. The detector was a Synapse CCD detector. Spectra were typically collected by averaging at least 8 acquisitions of 2-30 s duration. The Raman shift was calibrated using the Raleigh peak and the 520.7 cm^{-1} silicon line from an Si(100) reference sample. Spectra were baseline corrected using a linear fitting model. Samples were dropcast onto Si(100) wafers from methanolic suspension.

Raman spectra of PCC@SWNT

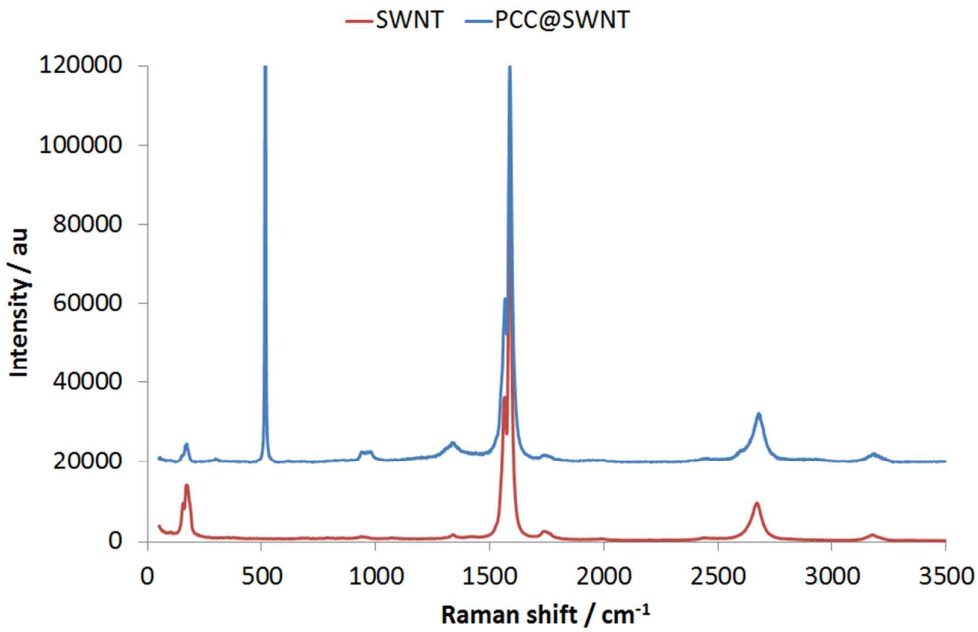

Figure S13. Raman spectra of SWNT (bottom, red line) and PCC@SWNT (top, blue line) recorded using the 532 nm laser. Spectra have been normalised to the intensity of the G band and shifted on the y-axis for clarity. Additional peaks at 300, 520 and 930 cm^{-1} in the spectra of PCC@SWNT correspond to known optical phonon modes in the Si(100) substrate.

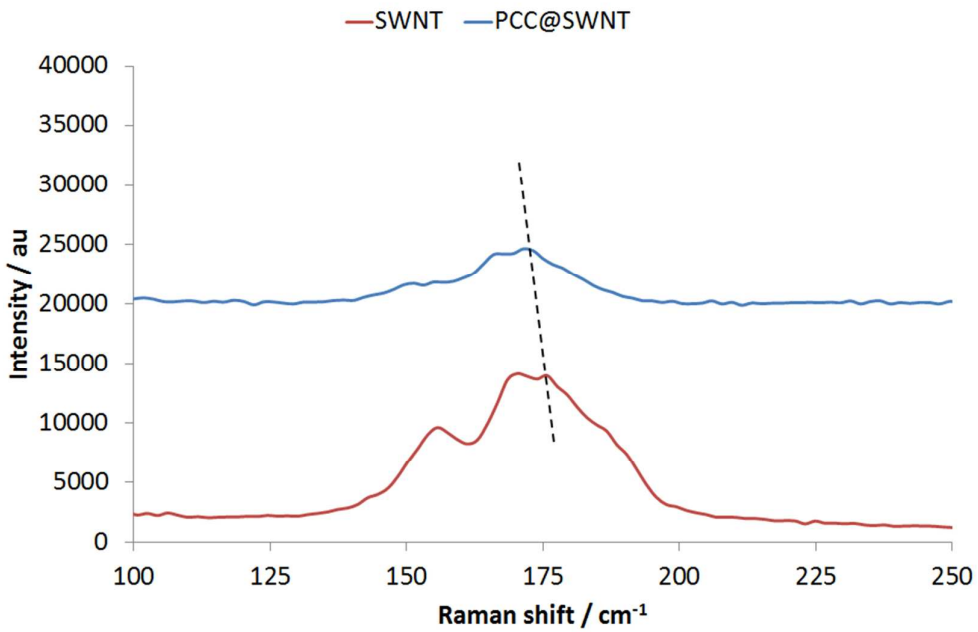

Figure S14. Raman spectra of SWNT (bottom, red line) and PCC@SWNT (top, blue line) recorded using the 532 nm laser in the region 100-250 cm^{-1} showing the small shift in at least one of the RBM subsequent to the encapsulation of PCC in SWNT. The dashed vertical line guides your eye to the shift in energy of the vibrational mode.

Subsequent to the encapsulation of PCC in SWNT, no change in the position of the G band was observed. However, a small shift from 174 to 171 cm^{-1} in the position of one of the RBM was noted (Figure S14). We tentatively ascribe these observations to the fact that the internal diameter of the subset of nanotubes that are in resonance with the 532 nm laser (which represents only a minor contribution to the total number of nanotubes present in the whole sample) is not large enough to accommodate the PCC molecule in a perpendicular orientation – the result being that there is insufficient interactions between PCC and SWNT to result in the transfer of electrons from PCC to SWNT or *vice versa*, as evidenced by no significant shift in the G band. The small decrease in the energy of one of the RBM (and decrease in intensity relative to the G band) is likely to be the result of a softening of this vibrational mode as the nanotube expands/distorts in an attempt to allow the PCC molecules to re-organise themselves in an orientation closer to the preferred perpendicular arrangement, where van der Waals contacts between PCC and SWNT are maximised. However, this does provide clear evidence that interactions do exist between PCC and SWNT, but these are weak and mediated predominantly by steric factors.

OTC@SWNT

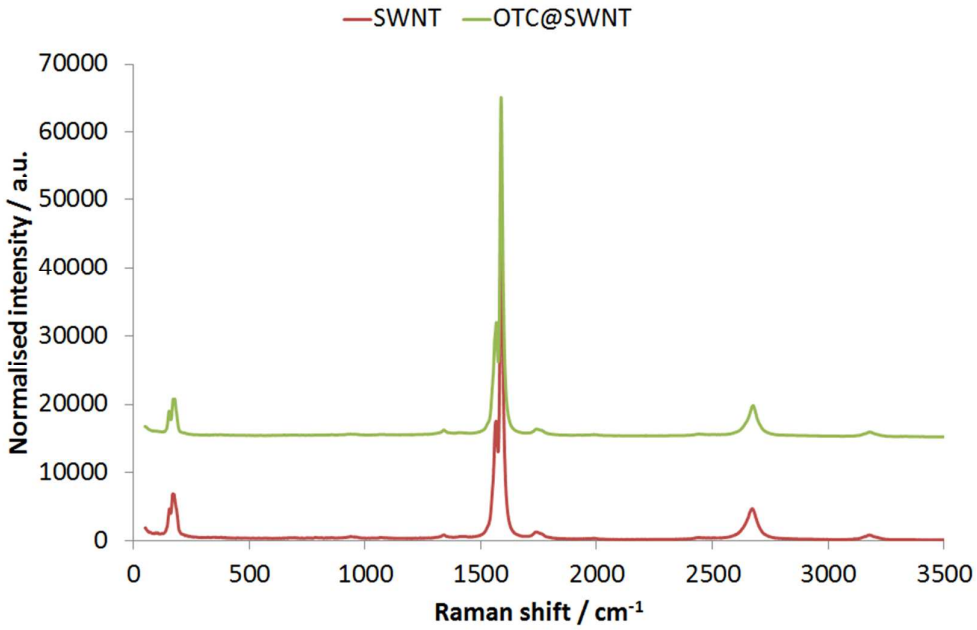

Figure S15. Raman spectra of SWNT (bottom, red line) and OTC@SWNT (top, green line) recorded using the 532 nm laser. Spectra have been normalised to the intensity of the G band and shifted on the y-axis for clarity.

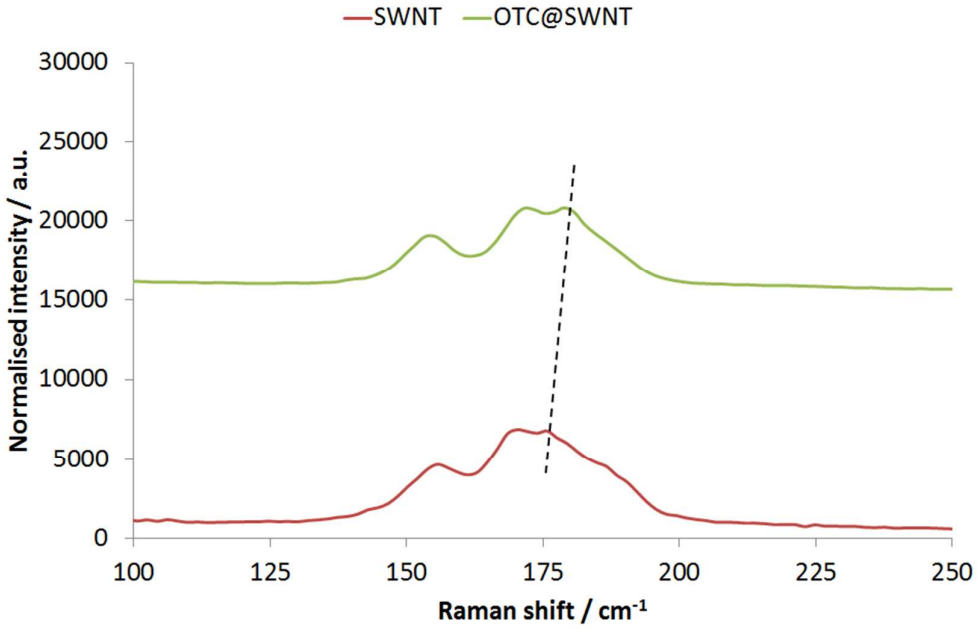

Figure S16. Raman spectra of SWNT (bottom, red line) and OTC@SWNT (top, green line) recorded using the 532 nm laser in the region 100-250 cm^{-1} showing the moderate shift in the position of at least one of the RBM subsequent to the encapsulation of OTC in SWNT. The dashed vertical line guides your eye to the shift in energy of the vibrational mode.

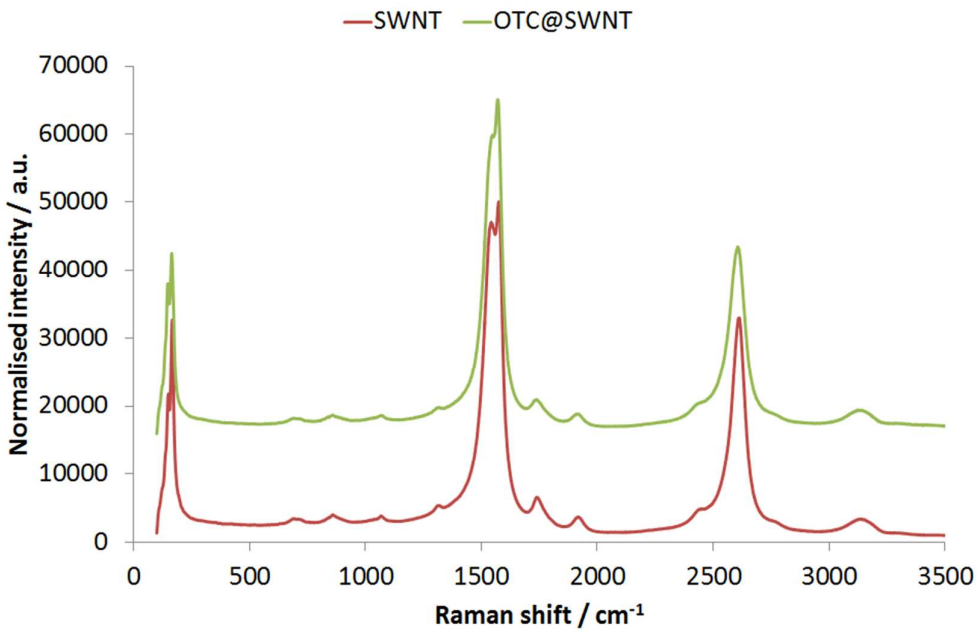

Figure S17. Raman spectra of SWNT (bottom, red line) and OTC@SWNT (top, green line) recorded using the 660 nm laser. Spectra have been normalised to the intensity of the G band and shifted on the y-axis for clarity.

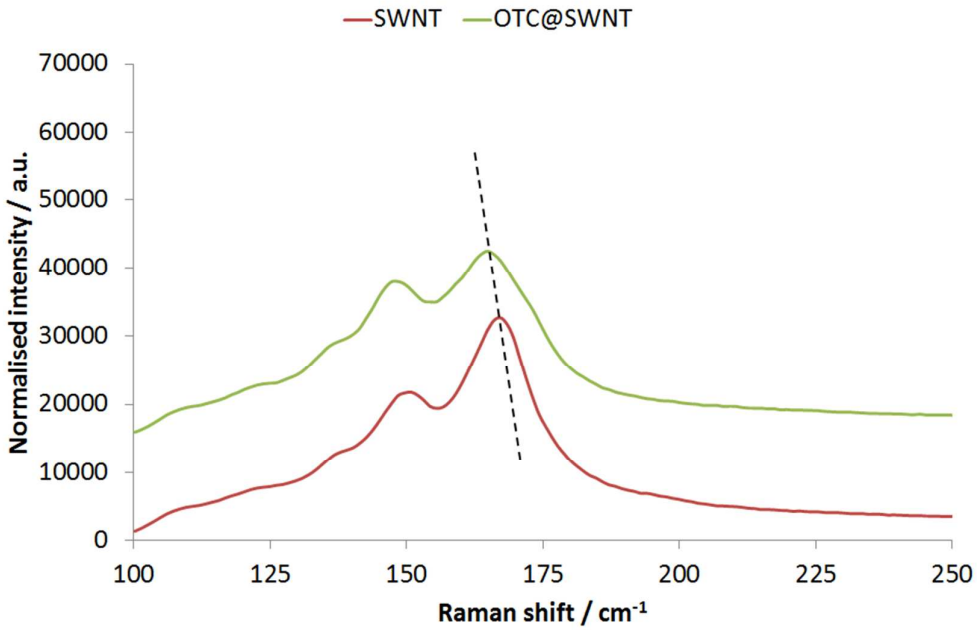

Figure S18. Raman spectra of SWNT (bottom, red line) and OTC@SWNT (top, green line) recorded using the 660 nm laser in the region 100-250 cm^{-1} showing the small shift in the position of at least one of the RBM subsequent to encapsulation of OTC in SWNT. The dashed vertical line guides your eye to the shift in energy of the vibrational mode.

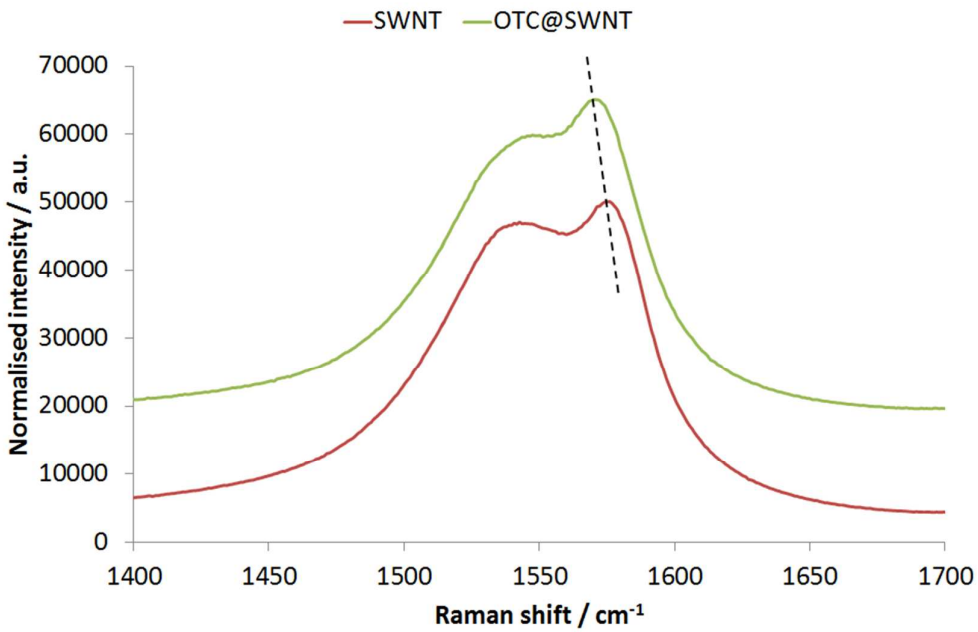

Figure S19. Raman spectra of SWNT (bottom, red line) and OTC@SWNT (top, green line) recorded using the 660 nm laser in the region 1400-1700 cm^{-1} showing the moderate shift in G band subsequent to encapsulation of OTC in SWNT. The dashed vertical line guides your eye to the shift in energy of the vibrational mode.

The vibrational properties of SWNT and OTC@SWNT were investigated using two lasers: 532 nm (Figure S15 and S16) and 660 nm (Figure S17, S18 and S19).

Using the 532 nm laser, we observe that subsequent to the encapsulation of OTC in SWNT, no change in the position of the G band was observed. However, a moderate shift from 174 to 181 cm^{-1} in the position of one of the RBM was noted (Figure S16). We tentatively ascribe these observations to the fact that the internal diameter of the subset of nanotubes that are in resonance with the 532 nm laser (which represents only a minor contribution to the total number of nanotubes present in the whole sample) is not large enough to accommodate the OTC molecule in a perpendicular orientation – the result being that there is insufficient interactions between OTC and SWNT to result in the transfer of electrons from OTC to SWNT or *vice versa*, as evidenced by no significant shift in the G band. However, the moderate increase in the energy of one of the RBM is likely to be the result of a contraction/distortion of the nanotube as it attempts to maximise the van der Waals surface contacts between OTC (in a non-perpendicular orientation) and the internal wall of the nanotube. This suggests that even though the interactions between OTC and SWNT are far from optimal in a non-perpendicular orientation of OTC, they are both present and strong, as evidenced by the recorded increases in the energy of the RBM mode.

Using the 660 nm laser, we observe that subsequent to the encapsulation of OTC in SWNT, a moderate shift in the position of the G band from 1576 to 1571 cm^{-1} was observed (Figure S18). Additionally, a small shift from 167 to 164 cm^{-1} in the position of the RBM was noted (Figure S19). We tentatively ascribe these observations to the fact that the internal diameter of the subset of nanotubes that are in resonance with the 660 nm laser (which represents a major contribution to the total number of nanotubes present in the whole sample) is large enough to accommodate the OTC molecule in a perpendicular orientation – the result being that there is significant electron

transfer from OTC (an electron-donor guest molecule) to SWNT (an electron-acceptor host nanostructure). The small decrease in the energy of the RBM is likely to be the result of a softening of this vibrational mode subsequent to encapsulation of OTC in SWNT and could be explained by either the expansion/distortion of the SWNT facilitating the arrangement of OTC in its optimal orientation or by doping effects.

The analysis and comparison of SWNT and OTC@SWNT using different laser excitation has clearly demonstrated that interactions between OTC and SWNT are strong and are influenced by both steric and electronic factors.

S9. X-ray Photoelectron Spectroscopy of PCC on graphene.

In order to confirm the identity of the molecules that appear as circles (face-on orientation) or lines (edge-on orientation) on graphene in AC-HRTEM images, X-ray Photoelectron Spectroscopy (XPS) measurements were carried out. The spectra demonstrate the presence of a Cl-peak thus confirming the identity of the molecules as PCC.

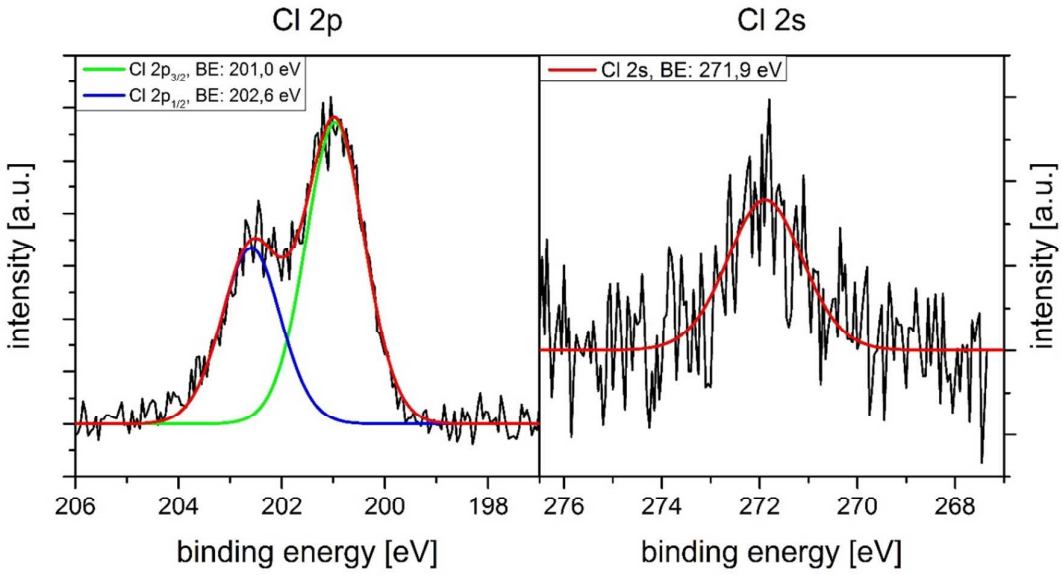

Figure S20. X-ray photoelectron spectra showing the presence of the characteristic Cl 2s and Cl $2p_{3/2,1/2}$ peaks after deposition of PCC molecules on a highly oriented pyrolytic graphite (HOPG) substrate. The intensity ratio $I(2p_{3/2}):I(2p_{1/2})$ is 2:1, as expected from the spin-orbit coupling if only one chemical species is present showing the adsorption of the chemically unaffected PCC molecules. The estimated coverage of PCC on the surface corresponds to about 1 %. HOPG substrates were used as test substrates for this experiment, as due to the micrometer sized free-standing areas of graphene on TEM grids the characterization of the adsorbed PCC on these samples by XPS was not possible.

S10. Heat-activated synthesis of nanoribbons from PCC in SWNT.

PCC@SWNT (10 mg) was sealed in a quartz glass ampoule under Ar atmosphere, and heated to 700°C, 800°C or 900°C for 24 h. The sample was then allowed to cool and analysed by TEM. Unlike the initial PCC@SWNT, no individual PCC molecules were observed in either of the thermally treated samples. Instead, ribbon-like structures (Figure S21a) were present in each sample confirming the

successful formation of Cl-GNR@SWNT in each case. The composition of the thermally evolved nanoribbons was confirmed to be similar to those formed under the 80 keV e-beam by EDX analysis (Figure S21b), but they appear to be consistently shorter due to partial PCC desorption from the nanotube during the heating process.

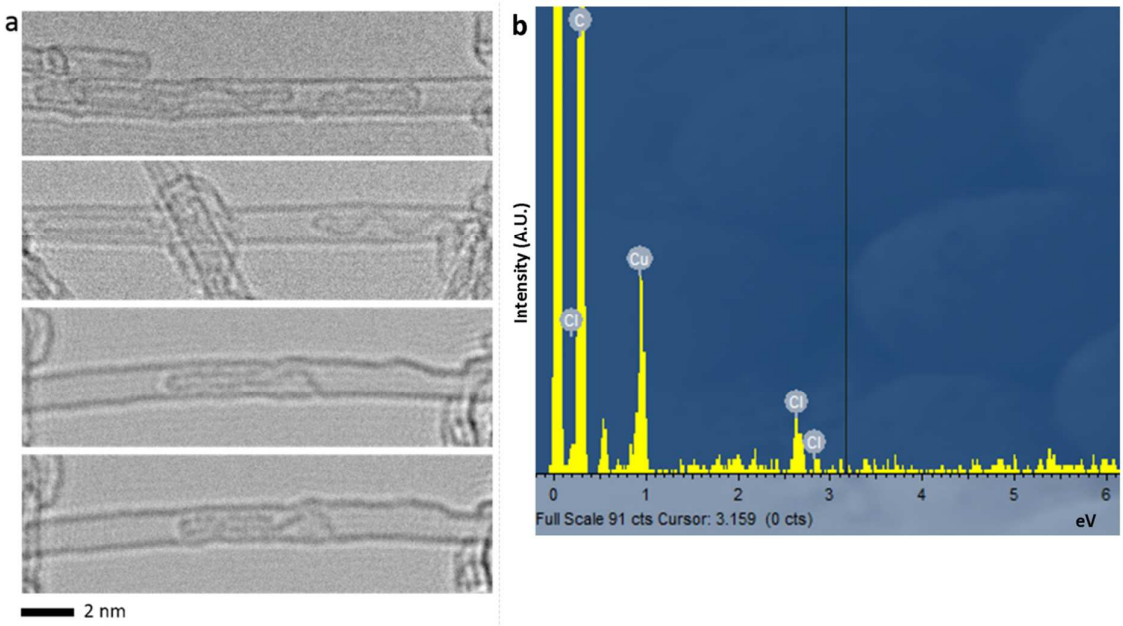

Figure S21. a) TEM images and b) EDX spectrum of Cl-terminated nanoribbons (Cl-GNR@SWNT) derived from PCC@SWNT upon thermal treatment at 900°C.

S11. Details of AC-HRTEM image simulations.

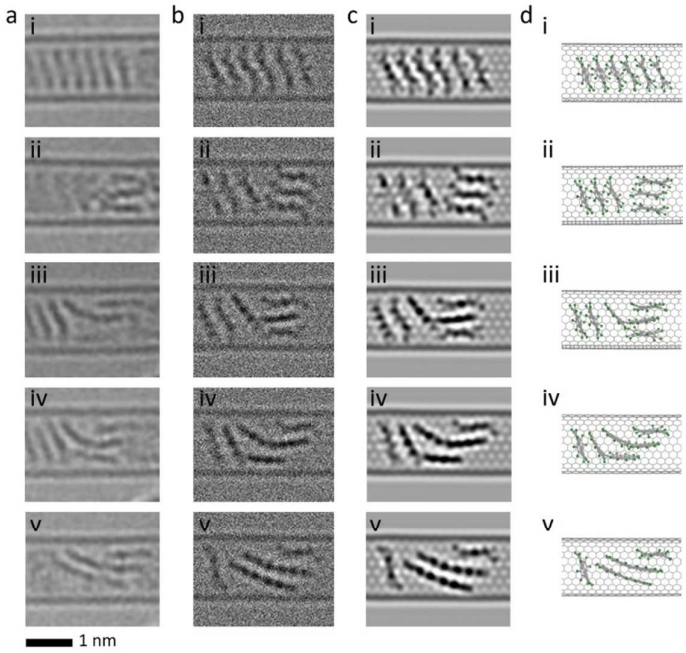

Figure S22. Time series of AC-HRTEM images at 80keV (ai-v) and corresponding simulated TEM images, generated by exposing structural models (di-v) to both limited (bi-v) and unlimited (ci-v)

electron doses, reveal how stacks of PCC molecules react overtime inside a SWNT. The images correspond to the TEM images shown in Figure 2b-d in the manuscript.

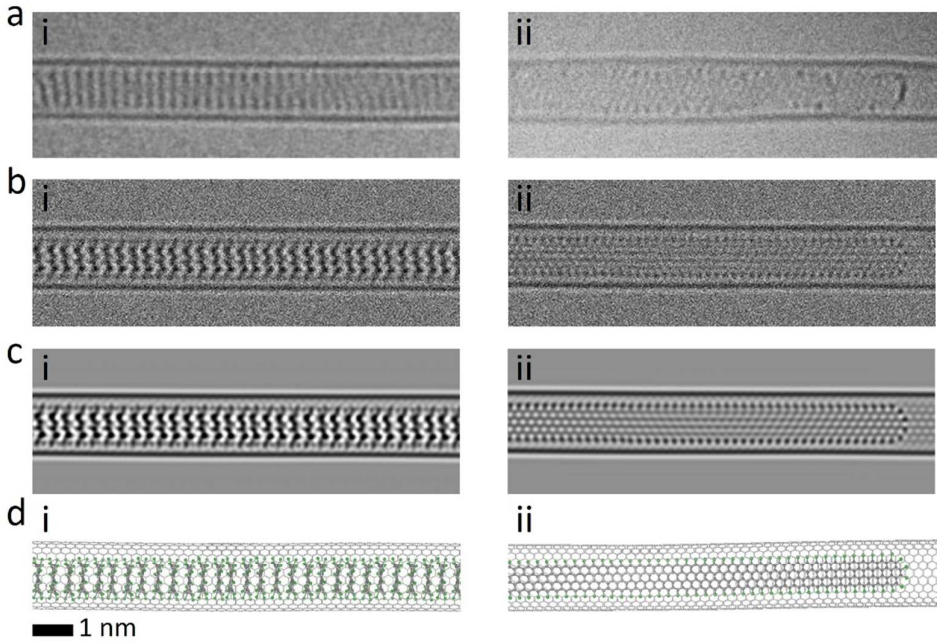

Figure S23. AC-HRTEM images at 80keV (ai-ii) and corresponding simulated TEM images, generated by exposing structural models (di-ii) to both limited (bi-ii) and unlimited (ci-ii) electron doses, showing the initial structure of PCC@SWNT (left) and the final Cl-terminated carbon nanoribbon inside the SWNT (right). The images correspond to the TEM images shown in Figure 3a-c in the manuscript.

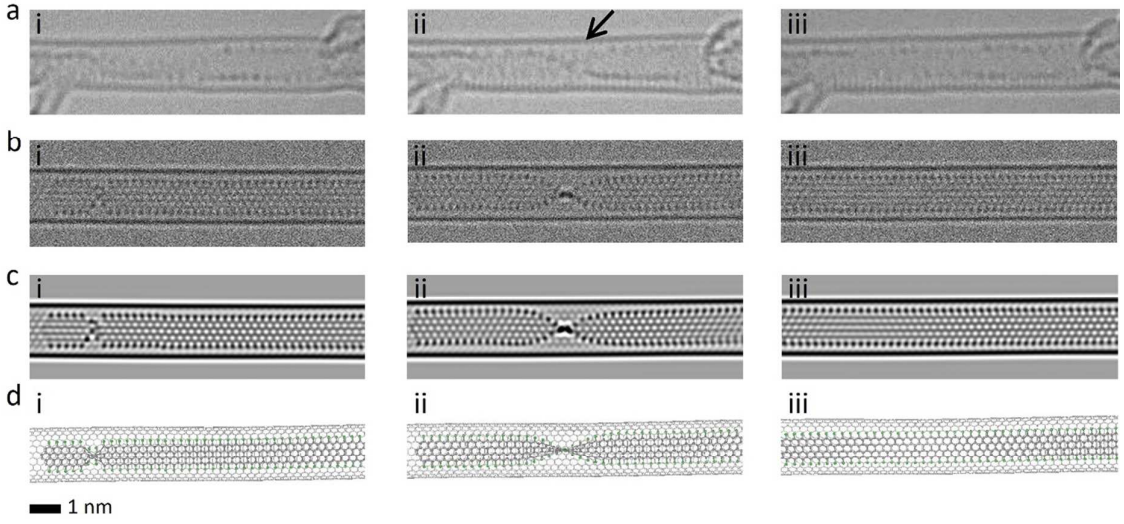

Figure S24. Time series of AC-HRTEM images at 80keV (ai-iii) and corresponding simulated TEM images, generated by exposing structural models (di-iii) to both limited (bi-iii) and unlimited (ci-iii) doses of 80 keV electrons, showing the dynamic behaviour of the Cl-terminated carbon nanoribbon inside the SWNT with the ribbon twisting and untwisting over time. The twist in the nanoribbon structure is highlighted with a black arrow. The images correspond to the TEM images shown in Figure 3h-j in the manuscript.

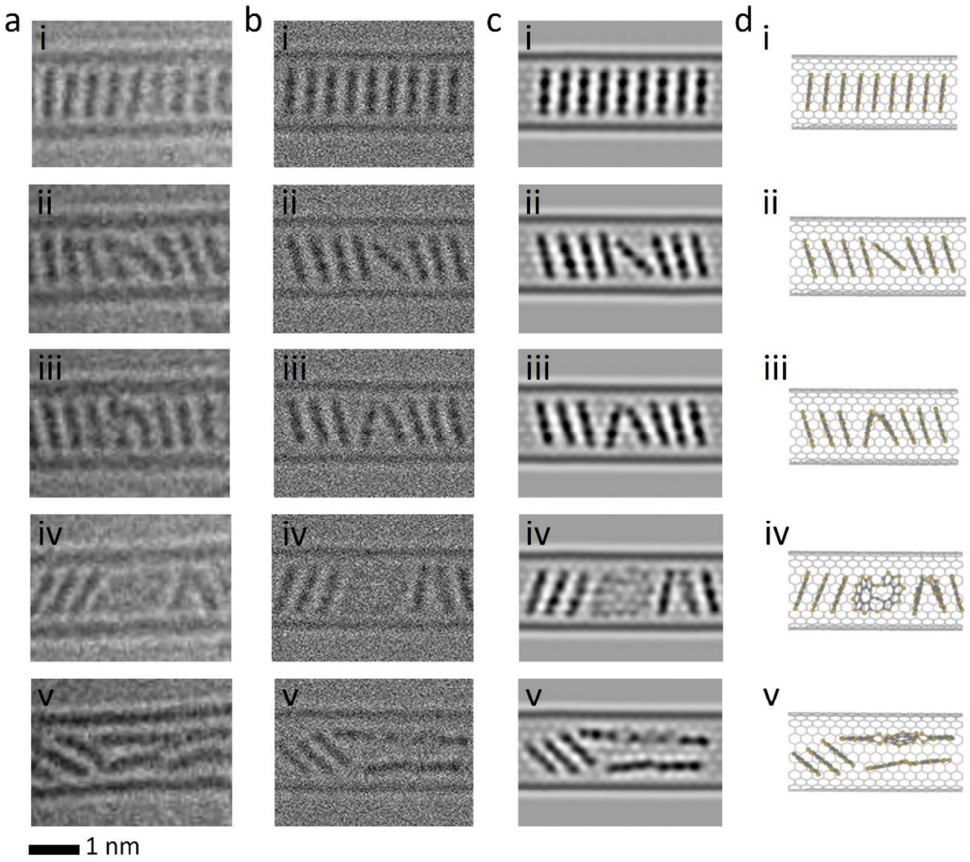

Figure S25. Time series of AC-HRTEM images at 80keV (ai-v) and corresponding simulated TEM images, generated by exposing structural models (di-v) to both limited (bi-v) and unlimited (ci-v) electron doses, reveal how stacks of OTC molecules react overtime inside a SWNT. The images correspond to the TEM images shown in Figure 5d-f in the manuscript.

References

1 Stone, A. J., Wales, D. J. Theoretical Studies of Icosahedral C_{60} and Some Related species. *Chem. Phys. Lett.* **1986**, *128*, 501–503.

2 Skowron, S. T., Lebedeva, I. V., Popov, A. M., Bichoutskaia, E. Approaches to Modelling Iirradiation-Induced Processes in Transmission Electron Microscopy. *Nanoscale*, **2013**, *5*, 6677.

3 T. Hensel, T. Andersen, N., Plesner, M., Pittelkow, M. Synthesis of Heterocyclic [8]Circulenes and Related Structures. *Synlett* **2015**, *27***,** 498–525.